Supporting Information Appendix for

Design Principles for Self-forming Interfaces Enabling Stable Lithium Metal Anodes

Yingying Zhu,[ꞁ, ꞁ] Vikram Pande,[⊥, ꞁ] Linsen Li,[ꞁ, †, *] Bohua Wen,[†] Sam Pan,[†] David Wang,[†] Zi-Feng Ma,[ꞁ] Venkatasubramanian Viswanathan,[⊥, *] Yet-Ming Chiang[†, *]

[ꞁ] Department of Chemical Engineering, Shanghai Electrochemical Energy Devices Research Center (SEED), Shanghai Jiao Tong University, Shanghai 200240, China

[†] Department of Materials Science & Engineering, Massachusetts Institute of Technology, Cambridge, MA 02139, USA

[⊥] Department of Mechanical Engineering, Carnegie Mellon University, Pittsburgh PA 15213, USA

[ꞁ] These authors contributed equally to the work.

* Corresponding authors: Linsen Li, Venkatasubramanian Viswanathan, Yet-Ming Chiang
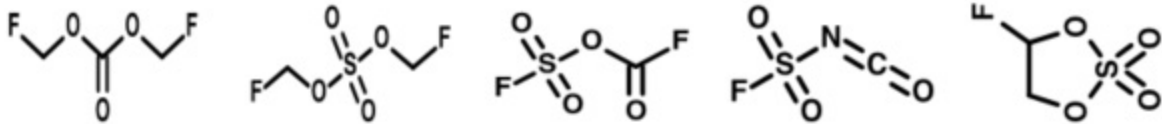
Email: linsenli@sjtu.edu.cn, venkvis@cmu.edu, ychiang@mit.edu
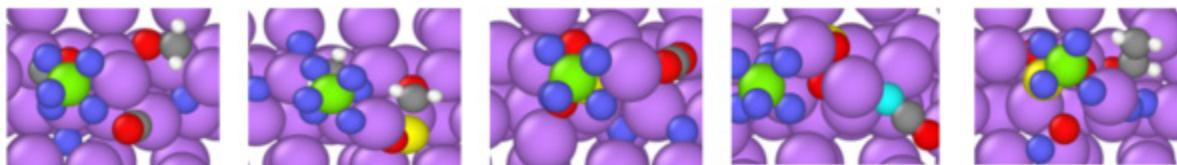
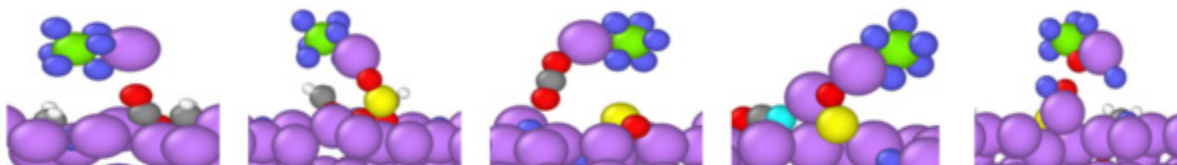**This PDF file includes:**
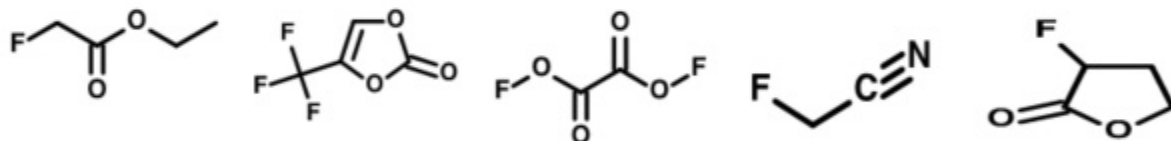
Figures S1 to S14

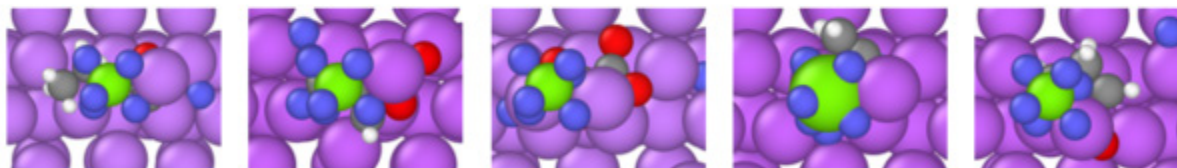Tables S1 to S3

Supplementary Text

1

Molecular Stuctures

Top View

Side View

Molecular Stuctures
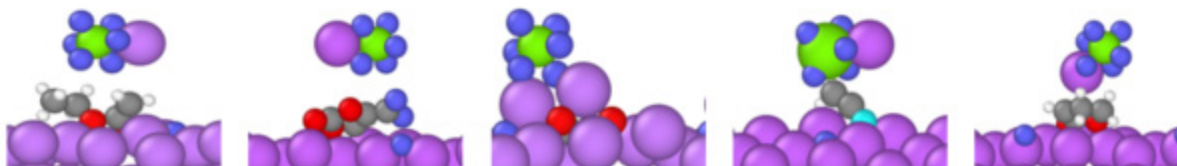
Top View

Side View

Molecular Stuctures

Top View

Side View
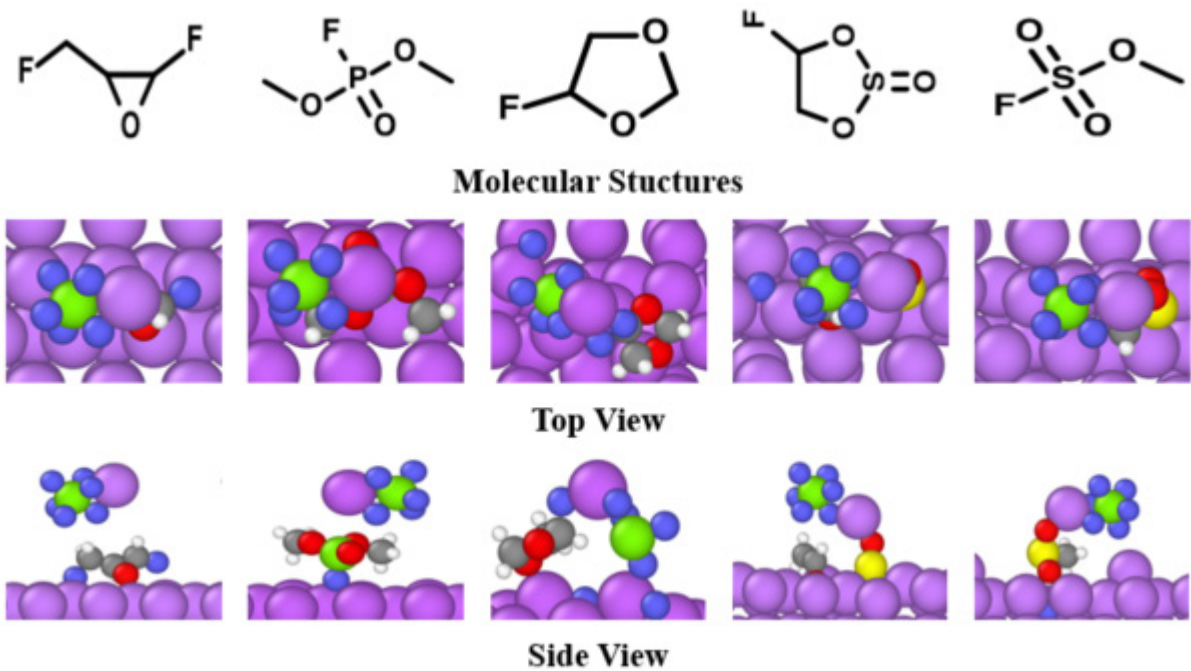
Figure S1 | Decomposition of fluorinated compounds at Li surface predicted by DFT calculations. We show here the decomposition of 15 compounds. Most fluorinated compounds do lead to the formation of LiF, but there are some compounds which do not release the fluorine such as fluorinated epoxides, ethers and compounds with CF_3 and CF_2 groups. We also see that some compounds such as fluorinated DTD, fluorinated dioxane lead to the formation of additional LiF by decomposing the $LiPF_6$ salt. Lastly all sulfate and sulfur groups decompose readily to form SO_2^{2-} anion which we believe would ultimately lead to the formation of Li_2SO_3 and $ROSO_2Li$.
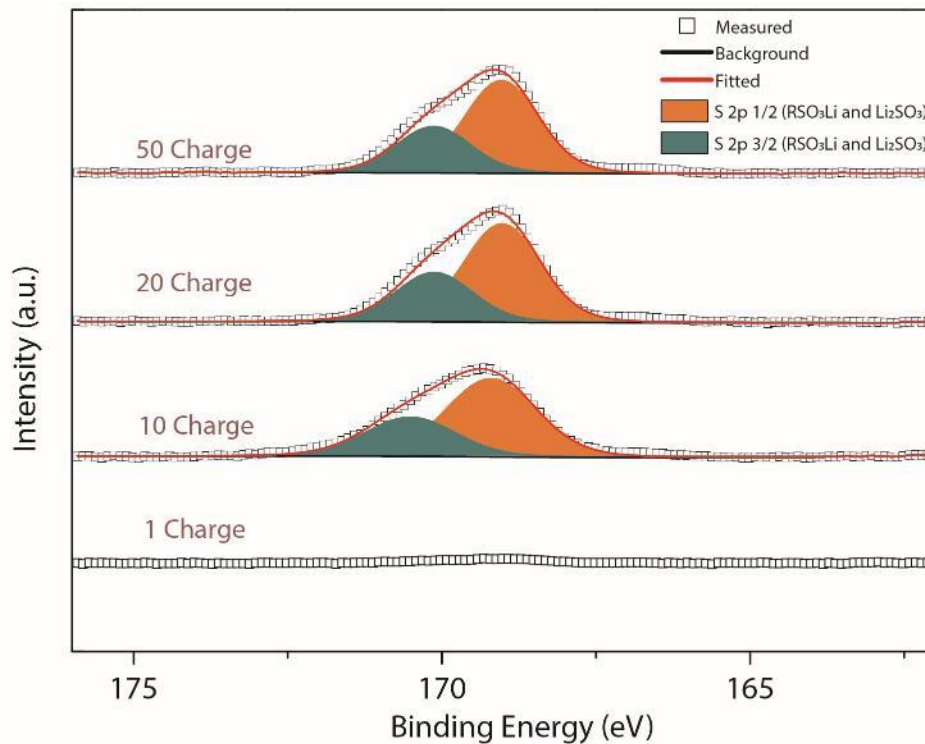
Figure S2 | Narrow-scan XPS spectra of S 2p and peak analysis. Narrow-scan XPS spectra of S 2p collected from the SEI formed on the Li electrode surface at the 1st charge, 20th charge, and 50th charge cycle. There is little S (0.1 at.%) in the SEI formed at the 1st charge according the wide-scan spectrum. S content increases to ~2 at.% at the 10th (~2.2 at.%), 20th (~1.7 at.%) and 50th charge (~2.0 at.%), respectively. The S 2p spectra was fitted using a spin-orbit split peak in relative ratio of 1:2 and binding energy difference of 1.2 eV. RSO_3Li and Li_2SO_3 are present in the SEI
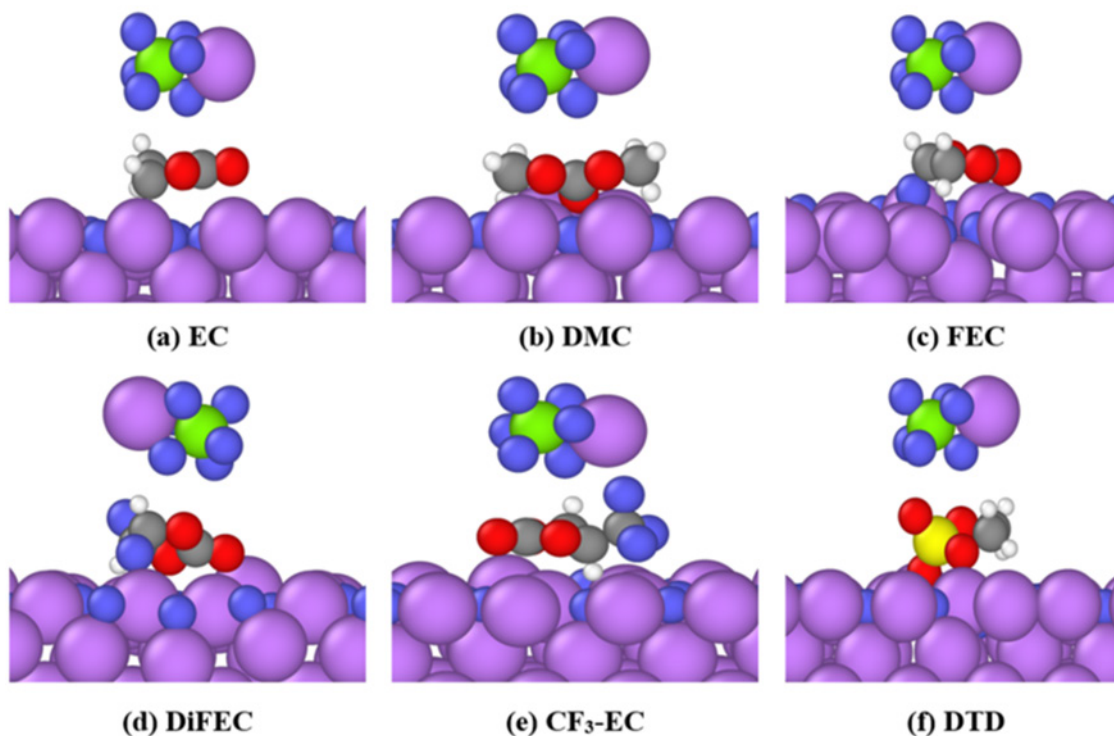
Figure S3 | Decomposition of solvent molecules on Li(100) surface with one mono layer of LiF. The pink atoms represent Li, red represent O, grey represent C, green represent P, purple represent F, yellow represent S and white represent H. There is no chemical decomposition of the solvent in any of the cases. This is also validated from the electrons transferred from the Li slab which is less than 0.5 electrons (0.3 for DMC, 0.2 for EC, 0.2 for FEC, 0.2 for DFEC, 0.1 for CF$_3$-EC, and 0.3 for DTD, respectively). Even in the case of DTD, the co-decomposition of DTD and LiPF$_6$ is stopped due to the unavailability of Li. This clearly shows that a monolayer of LiF is sufficient to chemically passivate a surface from further solvent decomposition (chemically). This proves that in general increased fraction of LiF in the SEI will lead to a more compact and dense SEI.
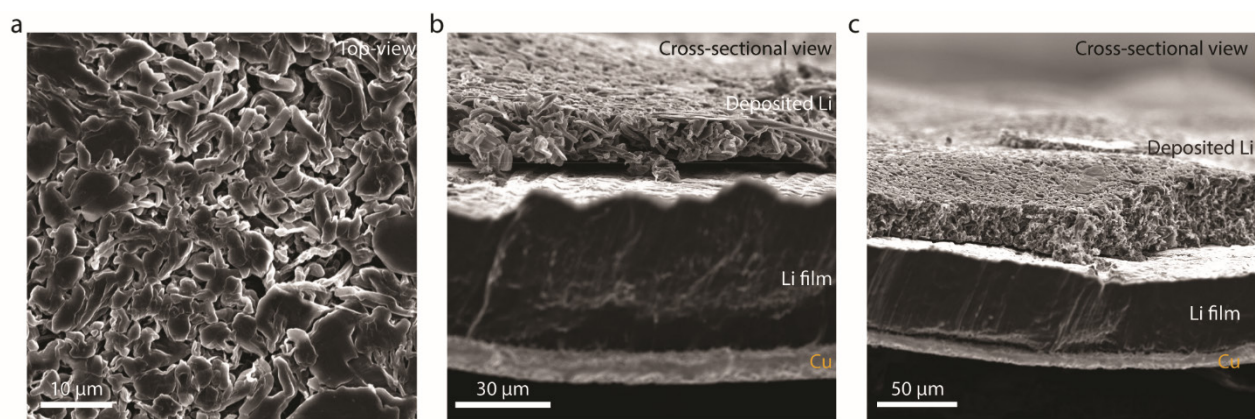
Figure S4 | SEM characterization of the deposited Li film on the Li/Cu substrates from Li-Li cells. a, Top-view SEM images of the deposited Li film on the Li/Cu substrates (50 µm-thick Li, 15 ▯m-thick Cu) in 1 M LiPF$_6$ EC-DMC (EL-0). The Li film was deposited in a Li-Li (thick Li foil vs 50 µm-thick Li on Cu) cell by charging at 0.42 mA cm^{-2} for 10 h. 4.2 mAh cm^{-2} of Li was deposited. More whisker-like Li particles were observed when a thick Li foil was used as the counter electrode instead of the roller-pressed LiCoO$_2$ electrode shown in Figure 3 of the main text. **b** and **c** are the corresponding cross-sectional SEM images, showing a three-layer structure consisting of the deposited Li, the original 50 µm-thick Li, and underlying Cu substrate. The deposited Li film consisted of whisker-like Li particles and had a wave-like surface, making it difficult to measure the thickness of the deposited Li film. The surface of the Li films deposited using LiCoO$_2$-Li cells were more flat, as shown in Figure 3 of the main text.

0.5 C, 1.85 mA cm^{-2} 1 C, 3.7 mA cm^{-2} 2 C, 7.4 mA cm^{-2}
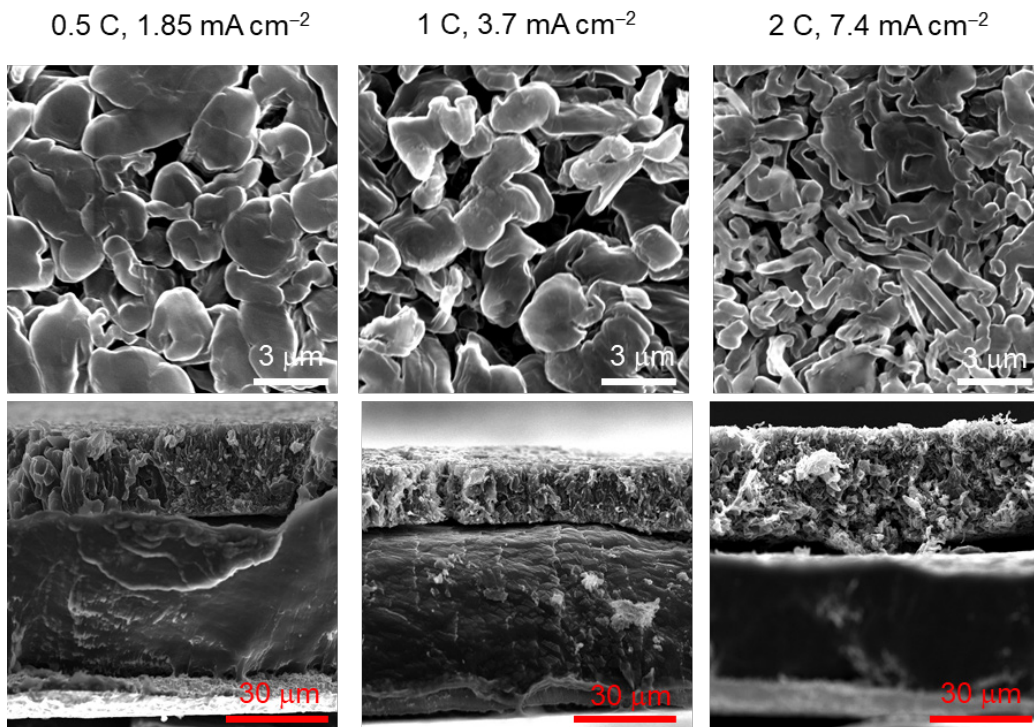
Figure S5 | SEM characterization of the deposited Li film on the Li/Cu substrates. The top three images are top-view SEM micrographs of the deposited Li films on the Li/Cu substrates (50 µm-thick Li, 15 µm-thick Cu) in 1 M LiPF$_6$ FEC-DMC + DTD (EL-4) The Li films were deposited in LiCoO$_2$-Li cells by charging to 4.5 V vs Li$^+$/Li at 0.5 C, 1, and 2 C rate (1 C = 3.7 mA cm^{-2}). The bottom three images are the corresponding cross-sectional SEM images. As the current density increases, the size of the deposited Li particles becomes smaller. The Li particles become more fiber-like as well.
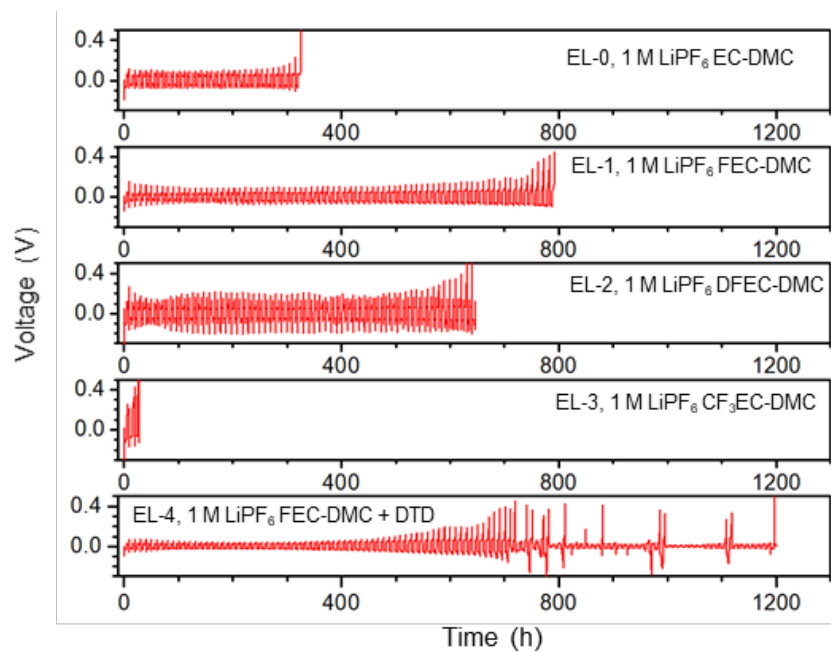
Figure S6 | Voltage curves of Li-Li asymmetric cell tests using EL-0, 1, 2, 3, and 4 electrolytes. The cycling current density was 0.6 mA cm^{-2}. The cycling area-capacity is 3.0 mAh cm^{-2}. Li was first deposited on the thin Li electrode and then stripped. The final voltage spikes denoted by the black arrows indicate the end of the tests when there is no Li available for stripping anymore and the absence of short-circuits during the tests. The tests were stopped when stripping voltage reached 0.5 V.

a — Li-Li asymmetric cell test results under 5, 30, 60, and 100 PSI stack pressure.

5 PSI

$CE_{avg-Li} = 1 - 6.18/(3\times102) = 98.0\%$
$CE_{avg-Li} = 1 - 6.18/(3\times106) = 98.1\%$ $98.07 \pm 0.08\%$
$CE_{avg-Li} = 1 - 6.18/(3\times113) = 98.2\%$

5 Psi

30 PSI

$CE_{avg-Li} = 1 - 6.18/(3\times155) = 98.7\%$
$CE_{avg-Li} = 1 - 6.18/(3\times149) = 98.6\%$ $98.63 \pm 0.03\%$
$CE_{avg-Li} = 1 - 6.18/(3\times146) = 98.6\%$

30 Psi

60 PSI

$CE_{avg-Li} = 1 - 6.18/(3\times214) = 99.0\%$
$CE_{avg-Li} = 1 - 6.18/(3\times175) = 98.8\%$
$CE_{avg-Li} = 1 - 6.18/(3\times167) = 98.8\%$ $98.88 \pm 0.12\%$

60 Psi

100 PSI

$CE_{avg-Li} = 1 - 6.18/(3\times176) = 98.8\%$
$CE_{avg-Li} = 1 - 6.18/(3\times176) = 98.8\%$
$CE_{avg-Li} = 1 - 6.18/(3\times225) = 99.1\%$ $98.91 \pm 0.12\%$

100 Psi

b

10 um thick copper
1.5 mm thick lithium
20 um thick PE separator
30 um thick lithium
10 um thick copper

Electrode stack assembly and dimensions.
Lithium active area is 50 mm x 36 mm.

Assembled cell ready for testing

Figure S7 | Li-Li asymmetric cell tests using pouch cells under stack pressure. a, Li-Li asymmetric cell test results from pouch cells under 5, 30, 60, and 100 PSI stack pressure. Three cells were tested in each case. **b,** Schematic illustration of the cross-section of the pouch cells and a digital photo of the cell.
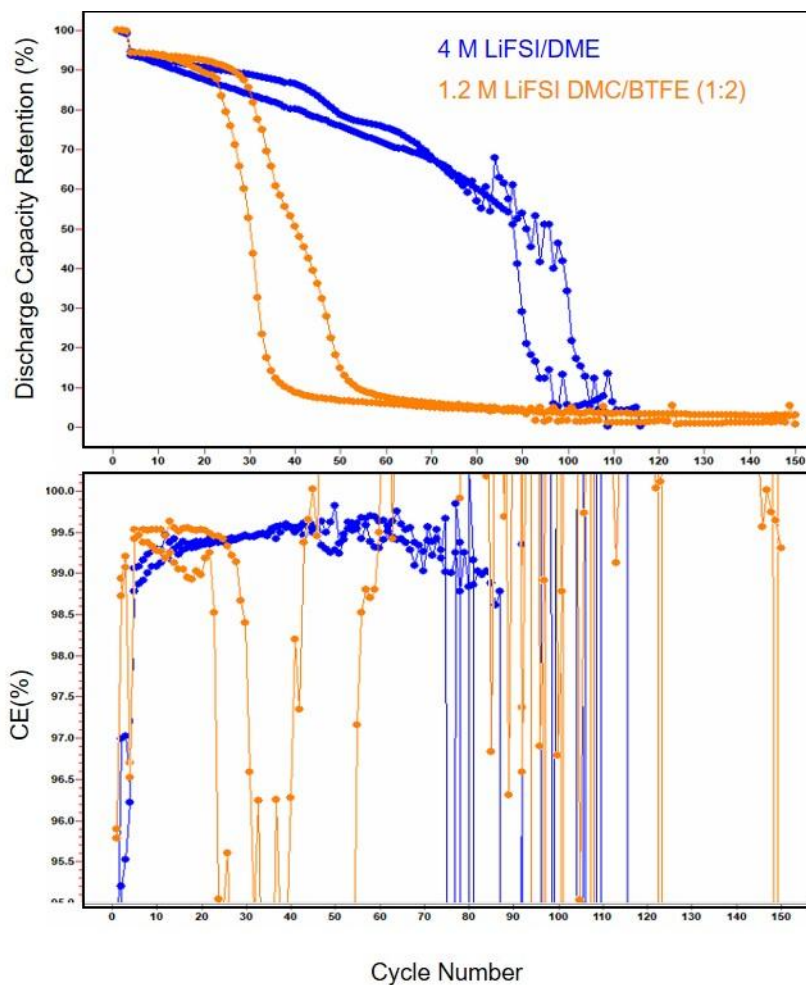
Figure S8 | LiCoO₂-Li full cells cycled with (localized) high-concentration electrolytes. Capacity retention and Coulombic efficiency of Li(50 μm)||LiCoO$_2$ (4.2 mAh cm^{-2}) full cells (2 cells in each case) using 4 M LiFSI/DME and 1.2 M LiFSI DMC/BTFE (1:2) electrolytes. These two electrolytes showed high CE$_{avg-Li}$ measured by the 10-cycle average method described in Adams et al, *Adv. Energy Mater.* 2018, 8, 1702097 (98.6 ± 0.5% for 4 M LiFSI/DME; 99.1% ± 0.05% for 1.2 M LiFSI DMC/BTFE). However, they are not compatible with the high-voltage LiCoO$_2$ (4.5 V) cathode. LiCoO$_2$-Li cells showed rapid capacity decay in capacity and CE.

Figure S9 | Coulombic efficiency measured by Li-Cu cells. In each cycle, 1 mAh cm^{-2} of lithium is deposited onto a Cu substrate and then stripped at 1 mA cm^{-2} until the voltage reaches 1 V v.s. Li$^+$/Li.
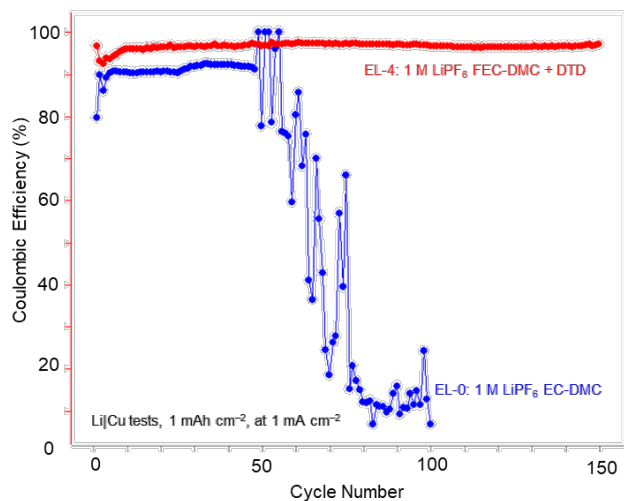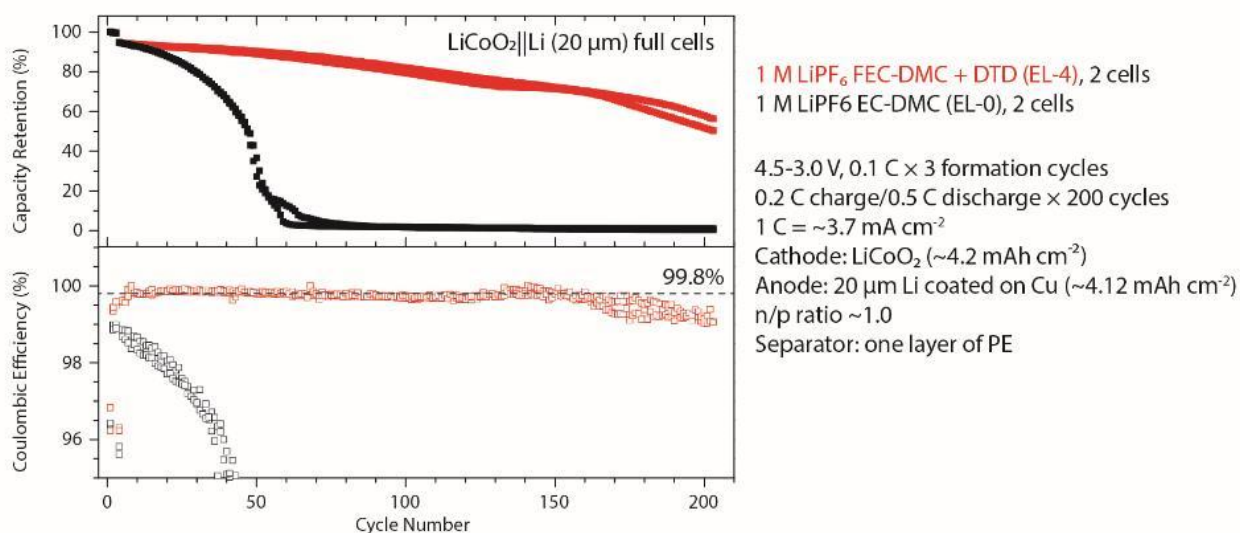
Figure S10 | Electrochemical tests of LiCoO$_2$-Li (20 μm) full batteries. The cycling performance (top panel) and CE (bottom panel) of the LiCoO$_2$-Li full cells using the EL-4 electrolyte (1 M LiPF$_6$ FEC-DMC + 3wt% DTD) shown in comparison with the control electrolyte (EL-0, 1 M LiPF$_6$ EC-DMC). The cells were first cycled at 0.1 C between 4.5-3.0 V for three cycles and then cycled at 0.2C charge/0.5 C discharge for 200 cycles. Data from two cells was shown in each case. The LiCoO$_2$||Li (20 μm) full batteries lasted more than 130 cycles (80% capacity retained, relative to the first 0.2C charge/0.5 C discharge cycle) and showed average CE ~99.8% before the capacity decreased to <80%.
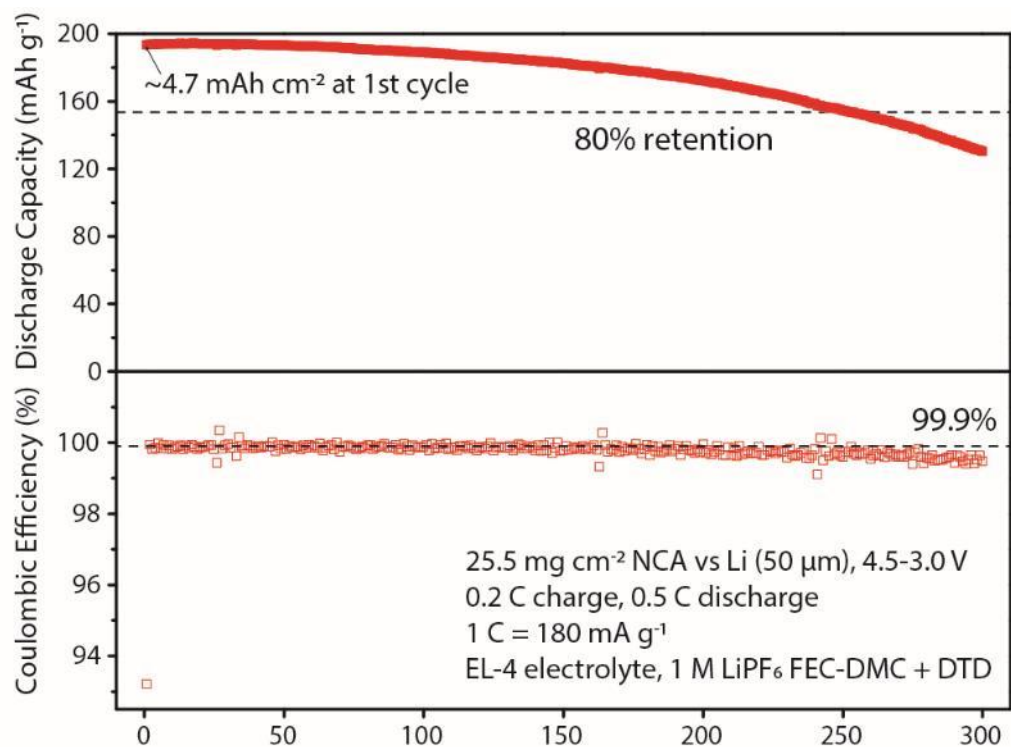
Figure S11 | Electrochemical tests of LiNi$_{0.8}$Co$_{0.15}$Al$_{0.05}$O$_2$-Li (50 μm) full batteries. The cycling performance (top panel) and CE (bottom panel) of a NCA-Li full cell using the EL-4 electrolyte (1 M LiPF$_6$ FEC-DMC + 3wt% DTD). The cells were first cycled at 0.1 C between 4.5-3.0 V for three cycles and then cycled at 0.2C charge/0.5 C discharge for 300 cycles. The data from 0.2C/0.5C cycling is shown. The NCA||Li (50 μm) full cell lasted more than 252 cycles (80% capacity retained, relative to the first 0.2C charge/0.5 C discharge cycle) and showed average CE ~99.9% before the capacity decreased to <80%. This data was used for Point 26 in Figure 6 of the main text.

Figure S12 | Electrochemical tests of Lithium-rich NMC-Li full cell. The cell is cycled at 0.2 C rate (1 C = 270 mA g^{-1}) between 4.85-2.0 V using the EL-4 electrolyte (1 M LiPF$_6$ FEC-DMC + 3wt% DTD). 20-cycle data is shown in this Figure. The lithium-rich NMC material is Li$_{1.19}$Ni$_{0.13}$Mn$_{0.54}$Co$_{0.14}$O$_2$.

(a) Li(100) (b) Li(110) (c) Li(111)

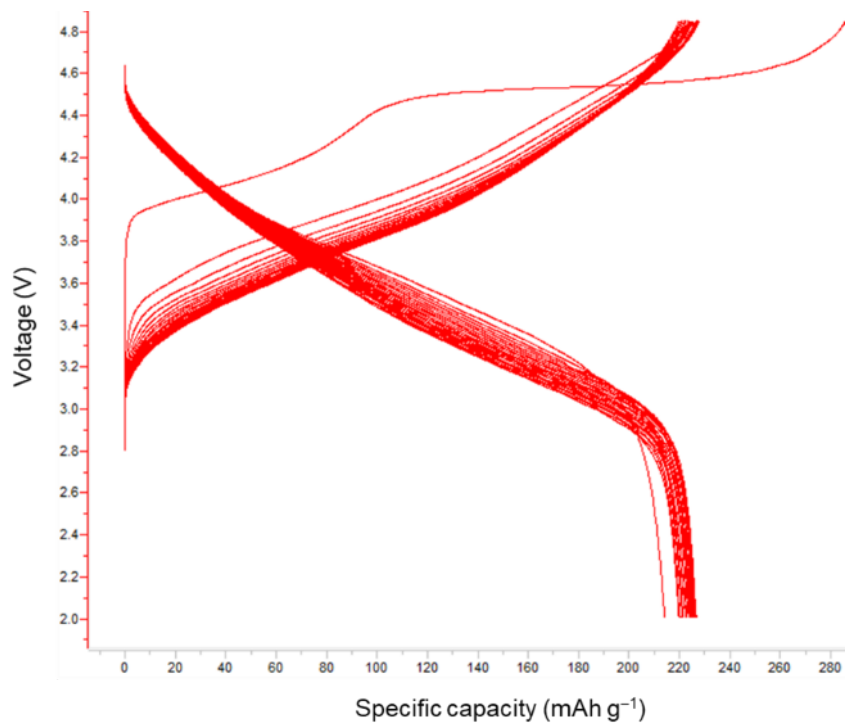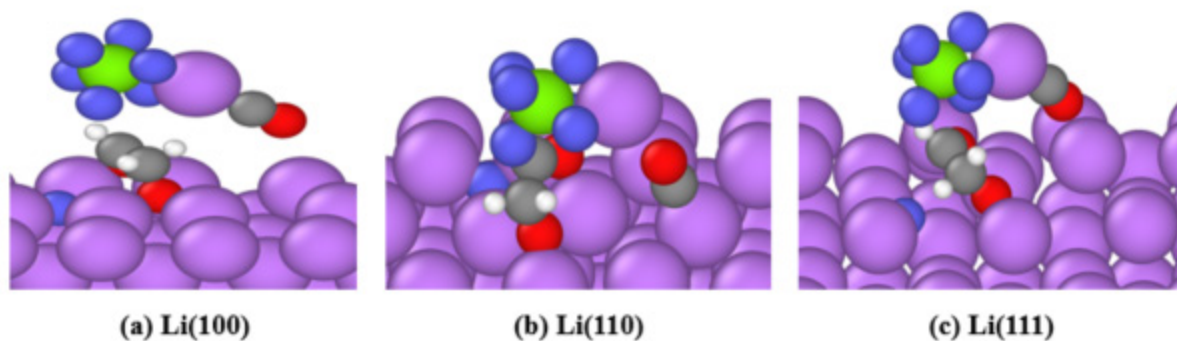**Figure S13 | Decomposition of FEC in the presence of LiPF₆ salt on Li (100), (110) and (111) surfaces**. The pink atoms represent Li, green represent P and purple represent F. The decomposition products are identical in all cases. We suggest that the surface energy effects do not significantly affect the decomposition pathway for solvent decomposition on Li. We also see identical results for other solvents considered in this study. We hypothesize that the reason behind this is surface energy difference between different surface ~0.2−0.5 eV while the energy difference is an order of magnitude higher for the decomposition reaction ~2−5 eV. This shows that even during SEI healing, the exposed Li cracks will react to give similar reaction products assuming there are sufficient free Li atoms to complete the decomposition. In some cases, it is possible that due to passivation, the complete decomposition does not happen.
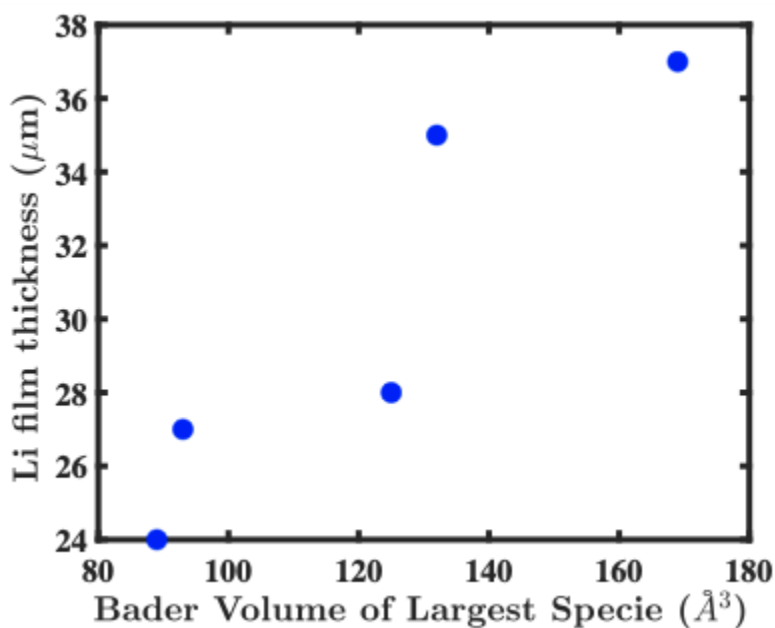
Figure S14 | Comparison of deposited Li film thickness and Bader Volume descriptor. The deposited film thickness was measured at the end of cycling using SEM and the Bader Volume was calculated using DFT.

Supplementary Tables

Table S1 | Percentage of different elements at the surface of the deposited Li in different electrolytes

	Electrolyte	C	O	F	Li	P	S
EL-0, 1st deposition	1 M LiPF6 EC-DMC	26.6	28.7	1.5	42.8	0.4	NA
EL-1, 1st deposition	1 M LiPF6 FEC-DMC	28.3	22	5.8	43.5	0.4	NA
EL-2, 1st deposition	1 M LiPF6 DFEC-DMC	33.2	19.3	10.6	36.5	0.4	NA
EL-3, 1st deposition	1 M LiPF6 CF3EC-DMC	13.6	34.1	1.7	50.6	0	NA
EL-4, 1st deposition		22.4	20.7	7.2	48.1	1.5	0.1
EL-4, 10th deposition	1 M LiPF6 FEC-DMC + 3wt% DTD	41.7	30.2	6.1	19.4	0.4	2.2
EL-4, 20th deposition		39.7	31.5	6.7	20.1	0.3	1.7
EL-4, 50th deposition		42.2	29.8	6.3	19.3	0.4	2

Table S2 | Average Coulombic efficiency of the thin Li anodes in different electrolytes

Lithium Salt (1 M)	Solvents & Additives	N	CE_{avg}
$LiPF_6$	PC	9	84.7%
LiTFSI	DOL-DME (1:1 v), 0.1 M LiI	14	90.2%
$LiPF_6$	EC-EMC (1:1 v)	24	94.3%
LiTFSI	EC-THP (1:1 v)	53	97.4%
$LiAsF_6$	EC-DMC (1:1 v)	58	97.6%
$LiAsF_6$	EC-2MeTHF (1:1 v)	66	97.9%
LiTFSI	DOL-DME (1:1 v), 1 wt% $LiNO_3$	71	98.1%

Test conditions: 0.6 mA cm^{-2} current density, 3.0 mAh cm^{-2} cycling areal capacity. PC = propylene carbonate, DOL = 1, 3-dioxolane, DME = 1,2-Dimethoxyethane, EMC = ethyl methyl carbonate, THP = tetrahydropyran, 2-MeTHF = 2-methyl tetrahydrofuran

Table S3 | Ionic conductivity of different electrolytes

No.	Electrolyte Formulation	Ionic Conductivity (mS cm^{-1})
EL-0	1M $LiPF_6$ EC-DMC (1:1 v)	12.41
EL-1	1M $LiPF_6$ FEC-DMC (1:1 v)	10.21
EL-2	1M $LiPF_6$ DFEC-DMC (1:1 v)	Not measured due to limited amount of electrolyte
EL-3	1M $LiPF_6$ CF_3EC/DMC (1:1 v)	8.77
EL-4	1M $LiPF_6$ FEC-DMC + DTD (1:1 v)	10.29

Note: The conductivity of EL-2 (1 M $LiPF_6$ DFEC-DMC) was not measured because we were not able to obtain DFEC in a large quantity. We were only able to prepare 5 g of EL-2 versus 100 g for all the other electrolytes that we used. We suggest that the conductivity of EL-2 should be comparable to the other four electrolytes (approximately 8–10 mS cm^{-1}) based on the polarization curve of the Li-Li asymmetric cell using EL-2 electrolyte shown in **Figure S6**.

Dataset S1 is a separate Microsoft Excel file

Dataset S1 | Additional information on the labeled points shown in Figure 6 of the manuscript.

Supplementary Text

DFT Calculation Details

Self-Consistent DFT calculations were performed using the real space projector-augmented wave method[1,2] implemented in the GPAW code[3,4] and employing the PBE exchange correlation functional[5]. We chose the Li (100), (110) and (111) surfaces for the DFT calculations. The Li surface comprised of four layers with the bottom two layers constrained at the bulk lattice constants. Each layer consisted of 3x3 Li unit cell. The solvent molecule was placed on top of Li surface at a distance of 2 Å. We explored different conformers of the solvent molecule, chosen based on placing electronegative atoms such as F and O close to the surface. Li$^+$ and PF_6^- ions were placed at a distance of 2 Å on top of the solvent molecule. LiPF$_6$ salt was placed for decomposition studies as it is known that salt ions affect the stability of solvent molecules by renormalizing the molecular energy levels of the solvent.[6,7] In addition, the salt ions may themselves participate in the reaction. It is worth highlighting that there are numerous possible configurations of the salt ions and solvent, we believe that given the consistency between the structures, trends in reactivity are well captured with this approach. The internal coordinates of these structures were allowed to relax to determine the decomposition products. Periodic boundary conditions were used for x and y directions and a vacuum of 10 Å was used in the z direction perpendicular to the surface on both sides of the slab. A real-space grid spacing of 0.16 Å was used and the Brillouin zone was sampled using the Monkhorst Pack scheme[8] with a k-point grid of (6×6×1). The calculations were converged to < 5meV accuracy with respect to k-points and grid spacing. A Fermi-Dirac smearing of 0.05 eV All simulations were converged to a force < 0.05 eV Å^{-1}. Bader analysis[9] was used to determine the amount of charge transferred from the lithium to the solvent during the decomposition and also volumes of the various decomposed species.

Calculation of Bader Charges and Bader Volumes of different species

To calculate the Bader charges and volumes, initially the electron density as a function of spatial coordinates was stored in a ".cube" file. The Bader analysis was performed on the ".cube" file. For charges, the Bader analysis was done by setting the vacuum charge density to zero. This was done to ensure that all charges are assigned to the appropriate molecular species. For calculating Bader Volumes of the atoms, the Bader analysis was done by setting the vacuum charge density to 0.0001 e Å^{-3}. This was the error of the electron density in the DFT calculations performed. Thus, a cutoff lower than this value would not be consistent. A larger value for the vacuum charge density cutoff leads to incorrect assignment of the electrons to different atoms. We checked for some different values in the appropriate range and found that the Bader Volumes calculated scale with those chosen numbers, but the trends in the volumes of different species remain the same as shown in the table shown below. This means that the species with the largest Bader volume is invariant implying that the descriptor used will provide the correct trend for the classification problem. The Bader charge transferred to the solvent while decomposition was calculated as negative of the charge on the Li(100) slab because the overall system is charge neutral. The decomposed species

were identified by considering bond distances between two atoms. Two atoms were considered chemically bonded if the distance between them was less than 1.75 Å. Thus, all the decomposed species were identified and their charge and volumes calculated by summing over the charges and volumes of the individual atoms.

Solvent	Bader Volume ($Å^3$) for Cutoff Density		
	0.0001 ($e/Å^3$)	0.0005 ($e/Å^3$)	0.001 ($e/Å^3$)
DMC	145	120	107
EC	132	110	99
FEC	89	75	67
DiFEC	125	103	92
CF_3-EC	169	137	122
DTD	97	81	74

Passivation of Li(100) surface covered with LiF

In order to explore the extent of passivation by LiF, we performed calculations by placing a monolayer of LiF on a 6 layer Li(100) slab. The structure was generated by placing F atoms on top of the Li surface. After relaxation, this spontaneously led to the formation of a LiF monolayer and 5 layers of Li(100). For simulating solvent decomposition on this structure, the bottom two layers were constrained to the bulk lattice constant of Li and the other layers and the solvent molecule along with $LiPF_6$ was allowed to relax. A similar Bader charge analysis was done to determine the charge transferred to the solvent. This shows us whether there is any Li oxidation and hence any possible reaction with the solvent. If the charge transferred is less than 0.5 e⁻ then, this would indicate that the surface is passivated and no further reaction with the solvent is likely.

Rationale for descriptors

Descriptor 1: Electrons transferred: An important requirement for a stable SEI layer is the requirement that it is electronically insulating, preventing further reaction with the electrolyte and pathways for potential soft shorts. The first descriptor considered in the paper is the number of electrons transferred from Li(100) surface to the solvent. This descriptor provides a measure of the amount of ionic compounds such as LiF,

Li_2O, Li_2CO_3, etc. in the SEI and an indirect measure of the insulating nature of the SEI. Increase in the number of electrons transferred results in increased anion and Li^+ formation which clearly suggests that the resulting compounds in the SEI are more ionic in nature. In general, ionic compounds tend to have larger band gaps, which would imply low electronic conductivity. Putting all of this together, an increase in the amount of ionic compounds in the SEI implies that the SEI has a larger band gap and in turn, lower electronic conductivity. Low electronic conductivity leads to faster passivation i.e. lower smaller thickness of the SEI for limiting further reactions between Li and the electrolyte components. In addition ionic compounds also have higher shear moduli as compared to covalent compounds. Shear modulus is a critical property for dendrite suppression and hence uniform Li electrodeposition. A more uniform electrodeposition of Li anode implies lower side reactions and higher coulombic efficiency.

Descriptor 2: Bader Volume: Improving coulombic efficiency requires lowering lithium consumption through suppressing reactivity of the SEI and lowering the amount of dead lithium. The first descriptor addresses reactivity of the SEI. The second descriptor is chosen to address the microstructure of the SEI layer. The compactness of the SEI microstrucure can be used as an indirect measure of the SEI's capability to suppress formation of dead lithium and further SEI products. In addition, the microstructure also determines the Li^+ conductivity of the SEI. The microstructure of the SEI clearly depends on the size, shape and packing of the different compounds in the SEI. To a first approximation, we propose that volume of the largest SEI compound controls the microstructure of the SEI and this volume can be calculated using DFT as the Bader volume of the largest decomposed species in the SEI. In general, the larger bodies when packed together lead to the formation of larger pores. Now increased amount of pores in SEI will lead to the reduction of the overall mechanical stability of the SEI regions for the formation of dead lithium. Increased size of the pores also would lead to increased diffusion of solvent molecules which will be electrochemically reduced resulting in additional SEI formation. Another factor is that larger components in an SEI will mean that for the same area, there will be a lesser number of interfaces in the SEI which are critical for Li^+ transport. Given that the bulk phase of the SEI compounds are poor at conducting lithium ions, we expect that the conduction mechanism is dominant through the interfaces. Thus, the smaller the size of the components in the SEI, the more compact is the SEI leading to a more stable SEI microstructure having good Li^+ conductivity.

Calculation of Energy Density in Figure 1

	LCO mass (mg)	Separator mass (mg)	Li (mg)	Cu (mg)	Al (mg)	Electrolyte (mg)	Total Mass (mg)	Energy (Wh)	Energy Density (Wh/kg)	Total Volume (cm³)	Volumetric Energy Density (Wh/L)
LCO-Li (20um Li)	29.13	3.80	1.35	8.51	2.57	4.18	49.55	0.02156	370	0.0178	1029
LCO-Li (50 um Li)	29.13	3.80	3.38	8.51	2.57	4.18	51.58	0.02156	355	0.0216	848
LCO-Li (100 um Li)	29.13	3.80	6.76	8.51	2.57	4.18	54.96	0.02156	333	0.0280	656
LCO-Li (250 um Li)	29.13	3.80	16.91	8.51	2.57	4.18	65.10	0.02156	281	0.0470	390
LCO-Li (450 um Li)	29.13	3.80	30.44	8.51	2.57	4.18	78.63	0.02156	233	0.0723	253
LCO-Li (750 um Li)	29.13	3.80	50.73	8.51	2.57	4.18	98.93	0.02156	185	0.1103	166
LCO-Cu (anode free)	29.13	3.80	0.00	8.51	2.57	4.18	48.19	0.02156	380	0.0153	1199

		Capacity [mAh/g]	Density [g/cm³]	porosity	thickness [um]
Cathode	LCO	185	5	0.25	60
Anode	Lithium	3860		0	
Electrolyte	EC-EMC		1.2		
Current collector	Cu		8.96		15
	Al		2.7		15
Separator			1.2	0.5	25

Packaging factor = 0.85

Electrode area = 1.267 cm²

Supplementary References

[1] Blöchl, P. E., Projector augmented-wave method. *Physical review B*, 50(24), 17953 (1994).

[2] Kresse, G., & Joubert, D., From ultrasoft pseudopotentials to the projector augmented-wave method. *Physical Review B*, 59(3), 1758 (1999).

[3] Mortensen, J. J., Hansen, L. B., & Jacobsen, K. W., Real-space grid implementation of the projector augmented wave method. *Physical Review B*, 71(3), 035109 (2005).

[4] Enkovaara, J. E., Rostgaard, C., Mortensen, J. J., Chen, J., Dułak, M., Ferrighi, L. & Kristoffersen, H. H., Electronic structure calculations with GPAW: a real-space implementation of the projector augmented-wave method. *Journal of Physics: Condensed Matter*, 22(25), 253202 (2010).

[5] Perdew, J. P., Burke, K., & Ernzerhof, M., Generalized gradient approximation made simple.*Phys. Rev. Lett.*, 77(18), 3865 (1996).

[6] Kumar, N., & Siegel, D. J.. Interface-induced renormalization of electrolyte energy levels in magnesium batteries. *J. Phys. Chem. Lett.*, 7(5), 874-881 (2016)

[7] Khetan, A., Luntz, A., & Viswanathan, V.. Trade-offs in capacity and rechargeability in nonaqueous Li–O_2 batteries: Solution-driven growth versus nucleophilic stability. *J. Phys. Chem. Lett.*,, 6(7), 1254-1259 (2015)

[8] Monkhorst, H. J., & Pack, J. D. Special points for Brillouin-zone integrations. *Physical review B*, 13(12), 5188 (1976).

[9] Tang, W., Sanville, E., & Henkelman, G., A grid-based Bader analysis algorithm without lattice bias. *Journal of Physics: Condensed Matter*, 21(8), 084204 (2009).